ACS APPLIED MATERIALS & INTERFACES

www.acsami.org

Research Article

Tailoring Single Photon Sources in Hexagonal Boron Nitride via Chemical Vapor Deposition and Nanoscale Focused Ion Beam Milling

Rachael Klaiss, Joshua Ziegler, David J. Miller, Kara Zappitelli, Kenji Watanabe, Takashi Taniguchi, Sai Krishna Narayanan, Pratibha Dev, and Benjamín J. Alemán*

Cite This: https://doi.org/10.1021/acsami.5c16811

Read Online

ACCESS | Metrics & More | Article Recommendations | Supporting Information

ABSTRACT: Emerging quantum information technologies demand robust, tunable, single photon sources. Solid-state single photon emitters (SPEs) in the two-dimensional material hexagonal boron nitride (hBN) offer unique advantages, including stability and integration potential, yet current fabrication methods lack precise control over the emitter placement and properties. In this work, we demonstrate a high-yield approach to patterning SPE arrays in hBN by combining focused ion beam (FIB) milling with chemical vapor deposition (CVD) of nanocrystalline graphitic carbon. Using statistical design and analysis of experiments, we systematically map a high-dimensional parameter space—spanning FIB exposure and CVD conditions—to identify the optimal regimes for SPE formation and tunability. Our method leverages widely available fabrication tools and provides critical insights into defect activation mechanisms, offering a scalable, reproducible path toward controllable quantum emitter synthesis. Beyond hBN, this approach opens the door to generating defect-based SPEs in other low-defect solid-state materials. The result is a practical and versatile platform for creating quantum light sources tailored for applications in communication, sensing, and computation.

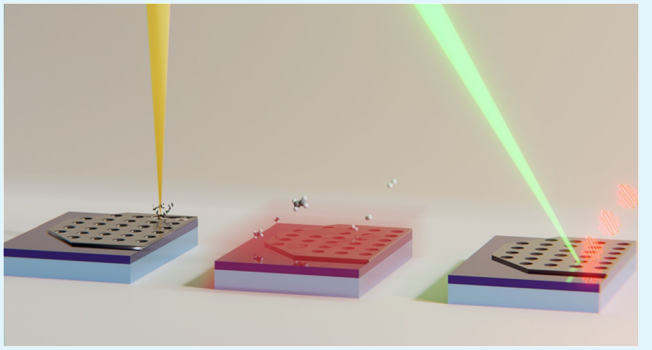

KEYWORDS: *solid-state single photon emitters, hexagonal boron nitride (hBN), focused ion beam (FIB) nanopatterning, chemical vapor deposition (CVD), defect engineering, quantum photonics integration*

Solid-state single photon emitters (SPEs) are essential for all-optical quantum computing, quantum communication, and fundamental quantum optics. The solid-state nature of these SPEs makes them desirable because of their ease of integration and potential for chip-level control and tunability.[1−5] SPEs in two-dimensional (2D) hexagonal boron nitride (hBN) have gained broad attention because they offer particularly straightforward integration, high brightness, strong surface-sensitivity, orders-of-magnitude wider range of strain-tunability than their bulk counterparts,[4,6,7] and robustness in ambient conditions.[8,9]

To integrate hBN SPEs into a chip device, however, it is essential that they be reproducibly patterned at well-defined positions.[2,3] There has been some success in large-scale activation of hBN SPEs with bulk focused ion beam (FIB),[10,11] plasma irradiation,[12] and carbon implantation,[13] but these methods generate randomly positioned single emitters or ensembles. Spatially resolved patterning of SPEs in hBN has been realized via electron beam irradiation[14] and nano-indentation.[15] In earlier work,[16] the authors patterned SPEs by milling nanoscale holes into hBN, but the reproducibility depended on material properties and even local variations of a given sample. For example, with otherwise identical process conditions, SPEs were patterned in lower-quality chemical vapor deposition (CVD) grown hBN contaminated with amorphous carbon, but never in pristine, exfoliated hBN.[16] Since carbon-vacancy centers are believed to be a dominant class of SPEs in hBN[17,18]—as supported by the activation of emitters via carbon implantation[13] and annealing in the presence of atomic carbon[19]—we use previous observations[16] to hypothesize that diffusive driving of carbon into vacancies located near edges of milled holes is a viable synthesis route for SPEs in hBN.

To test this hypothesis, we combined FIB nanopatterning with CVD deposition and thermally activated diffusion of carbon. Using this approach, we successfully nanofabricate patterned quantum emitters in hBN and use statistical factor

Received: August 25, 2025
Revised: November 17, 2025
Accepted: November 18, 2025

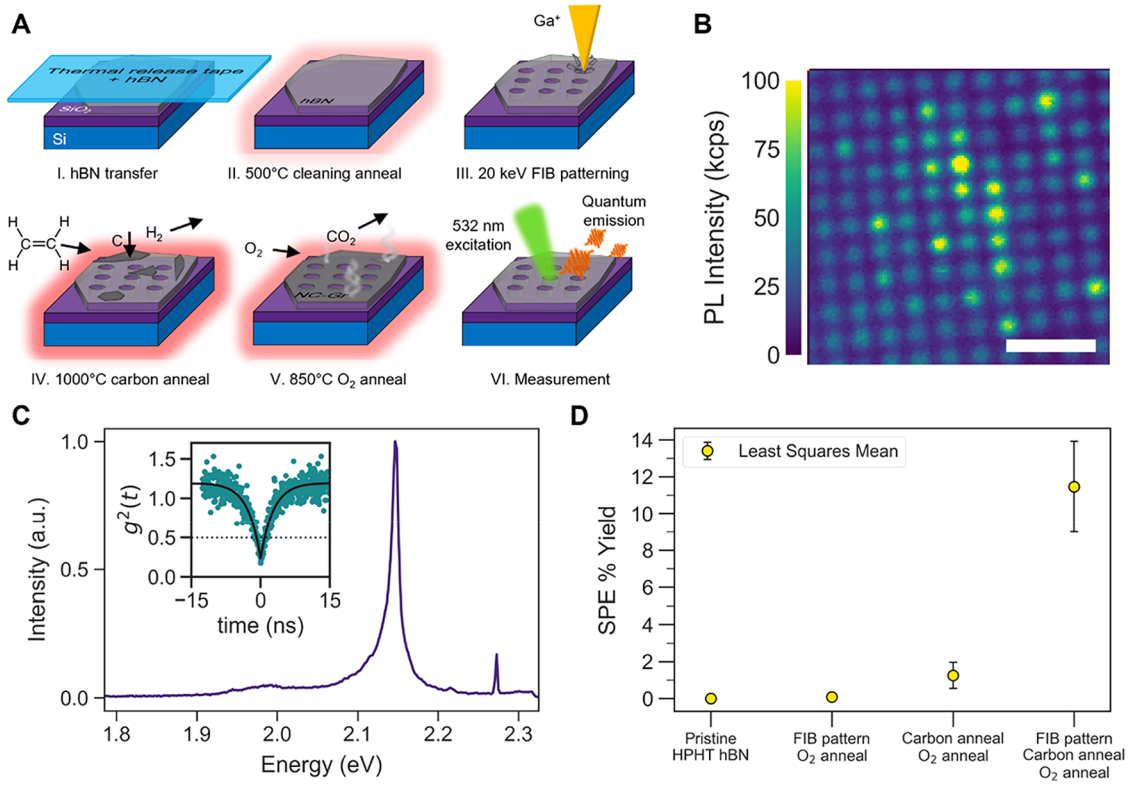

Figure 1. FIB patterning and carbon annealing to create SPEs in pristine hBN. (A) SPE fabrication process flow as described in the text. (B) Representative confocal PL map of a color center array on an hBN flake patterned with the described process. Dashed lines indicate hBN flake edges. Scale bar: 3 μm. (C) Zero-phonon line (ZPL) at ~2.15 eV and the corresponding phonon sideband (PSB) emission of 160 meV for a representative single photon emitter created with this process. Inset: $g^{(2)}(t)$ for the emitter with $g^{(2)}(0) = 0.24$, well below the $g^{(2)}(0) < 0.5$ threshold for single photon emission. (D) Yield of patterned sites that hosted single photon emitters on samples subjected to 4 different treatment combinations. Error bars show standard error on the mean.

screening to determine which process parameters and interactions govern SPE synthesis, which we then use to maximize the yield and tailor several photophysical properties of the hBN SPEs. We postulate that this process works when elemental carbon diffuses into vacancies created by FIB, entering at the edges from the surface of the hBN and perform process optimization experiments to confirm the viability of this model.

FABRICATION AND CHARACTERIZATION OF QUANTUM EMITTERS

The steps to fabricate samples used in this work are outlined in Figure 1A, with more details in the Methods section and Supporting Information. To create edge defects at deterministic locations, we patterned arrays of 500 nm circles separated by a 1 μm pitch using FIB with beam parameters determined in our previous work as optimal for SPE creation.[16,20] We then performed CVD of nanocrystalline graphite (NC-Gr) via noncatalytic ethylene decomposition at 1000 °C (confirmed via Raman spectroscopy; Figure S2), the annealing temperature shown to activate hBN SPEs in a carbon-rich environment.[19] To remove residual surface NC-Gr prior to characterization, we annealed the samples under flowing oxygen (see the Methods section).

We identified spots of photoluminescence (PL) and measured the degree of second-order coherence ($g^{(2)}(t)$) of emitted photons via a Hanbury-Brown-Twiss measurement in a home-built confocal microscope with 532 nm excitation [Figures 1B, andS3]. We use the accepted photon antibunching threshold for an SPE ($g^{(2)}(0) < 0.5$) to categorize emitting sites as an SPE [Figure 1C inset]. We denote any emitting site that exhibits partial antibunching (with $0.5 < g^{(2)}(0) < 1$) as a nonclassical light emitter (NLE). We categorize color centers as bright emitting sites that do not exhibit antibunching ($g^2(0) = 1$) and do not photobleach. We further characterized the quantum emitting nature of the spots by acquiring emission spectra, where we observed the expected zero-phonon line (ZPL) and corresponding phonon sideband (PSB) for quantum emitters [Figure 1C].

EFFECTS OF FABRICATION PARAMETERS ON SPE YIELD

The combination of FIB patterning and carbon annealing produced SPEs with a higher yield than only FIB patterning or only carbon annealing [Figure 1D]. The combined process (optimized parameters) yielded 0.115 ± 0.009 SPEs/μm^2, approximately 9.2× more SPEs than carbon annealing alone (0.013 ± 0.007 SPEs/ μm^2) [Table S2, t-test: $p < 0.0001$]. This observed difference in yield is in qualitative agreement with our density functional theory (DFT)-based calculations of the defect formation energies for a representative set of carbon-based defect complexes, which consist of substitutional carbon atoms adjacent to different vacancies. The formation energies of these defect complexes in pristine hBN are much larger than the energies required to incorporate carbon once vacancies have already been created in hBN [see Figure S14(A)]. The latter scenario emulates the experimental process of FIB followed by CVD.

https://doi.org/10.1021/acsami.5c16811
ACS Appl. Mater. Interfaces XXXX, XXX, XXX−XXX

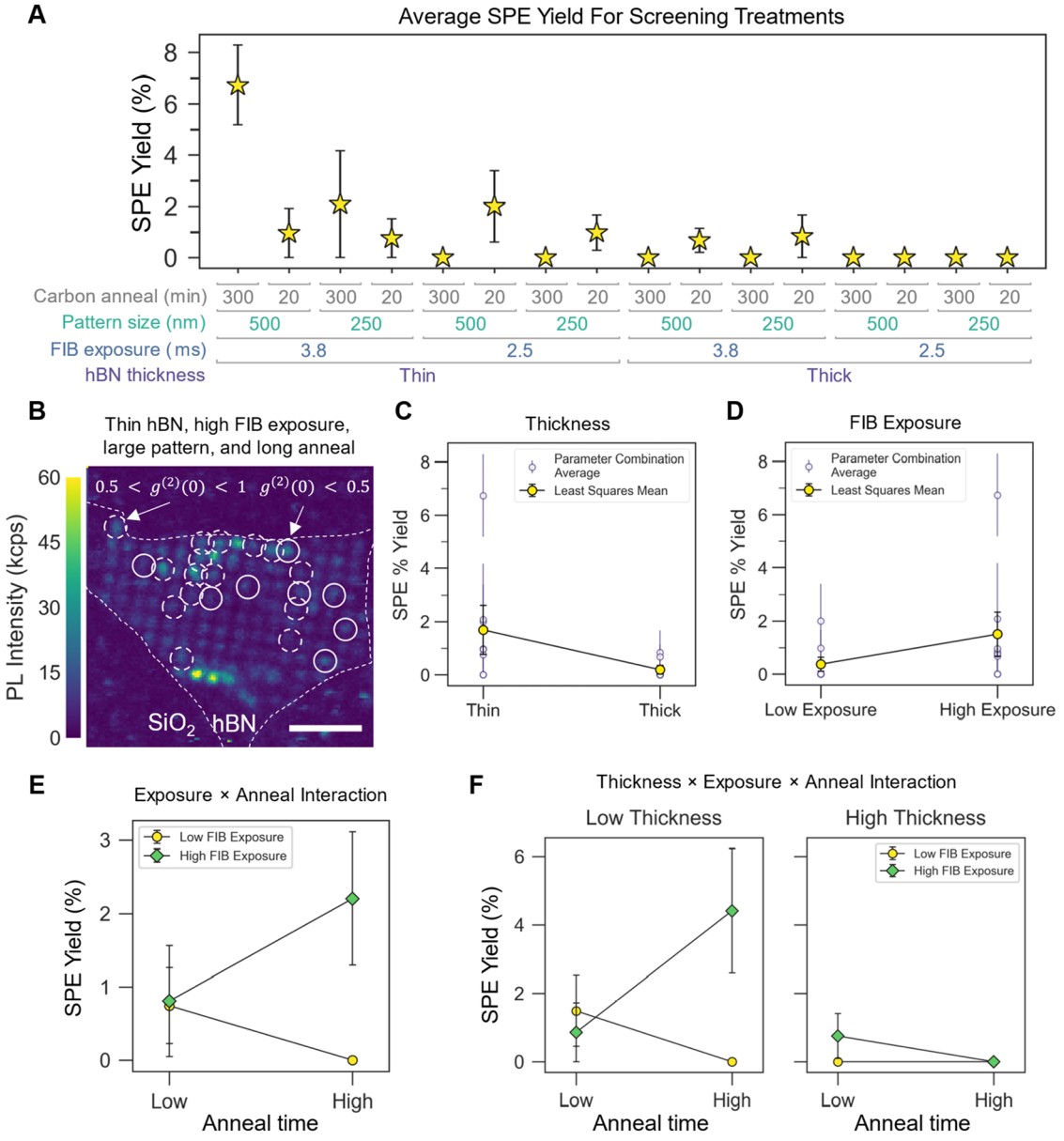

Figure 2. 4-Factor two-level screening. (A) SPE yield % for all screening treatments, with the highest SPE yield (Tukey-Kramer HSD) obtained for low thickness, high FIB pattern size, high FIB exposure time, and high carbon annealing time combination. (B) Confocal PL scan for a sample processed under the best conditions for SPE creation during factor screening. SPEs are circled in a solid white line, and NLEs are circled in a dashed white line. Scale Bar: 4 μm. (C, D) Single-factor effects. Open purple circles show the average SPE yield for each parameter combination. Error bars show standard error on mean. (C) Effect of the hBN thickness on the SPE yield. Closed yellow circles show least-squares mean SPE yield for thin hBN and thick hBN. Error bars show standard error on the mean. (D) Effect of the FIB exposure time on the SPE yield. Closed yellow circles show least-squares mean SPE yield for low exposure and high exposure. Error bars show standard error on the mean. (E) Effect of the FIB exposure-carbon annealing interaction on SPE yield. Closed yellow circles show least-squares mean SPE yield for low FIB exposure interactions and closed green circles show least-squares mean SPE yield for high FIB exposure interactions. Error bars show standard error on the mean. (F) Effect of the hBN thickness-FIB exposure-carbon annealing interaction on the SPE yield. The left panel shows thin hBN interactions, and the right panel shows thick hBN interactions. Closed yellow circles show least-squares mean SPE yield for low FIB exposure interactions and closed green circles show least-squares mean SPE yield for high FIB exposure interactions. Error bars show standard error on the mean.

To determine which fabrication parameters of the combined FIB-CVD technique contributed to the improved SPE yield, we performed a two-level screening factorial on four targeted factors: hBN thickness (14.59 ± 4.81, 28.47 ± 5.42 nm), FIB pattern size (250, 500 nm), FIB exposure time (2.5 ms, 3.8 ms), and carbon annealing time (20, 300 min) [Figure S4]. The parameter combination from this factor screening that produced the highest SPE yield was: 500 nm pattern diameter holes exposed for 3.8 ms on a 16 nm flake with 5 h of carbon annealing [Figure 2A,B]. Samples fabricated with this combination of parameters yielded 0.067 ± 0.006 SPEs per patterned site, which was 3.4× higher than the second-best parameter combination [Table S4, *t*-test: $p = 0.002$].

When analyzing the main (single-factor) effects, we found that hBN thickness had the strongest influence on SPE yield. Thinner flakes hosted 9.1× higher SPE yields than thicker flakes, regardless of the chosen FIB exposure time, pattern size, and carbon annealing time [Table S5 *F*-test: $p = 0.004$] [Figure 2C].

https://doi.org/10.1021/acsami.5c16811
ACS Appl. Mater. Interfaces XXXX, XXX, XXX−XXX

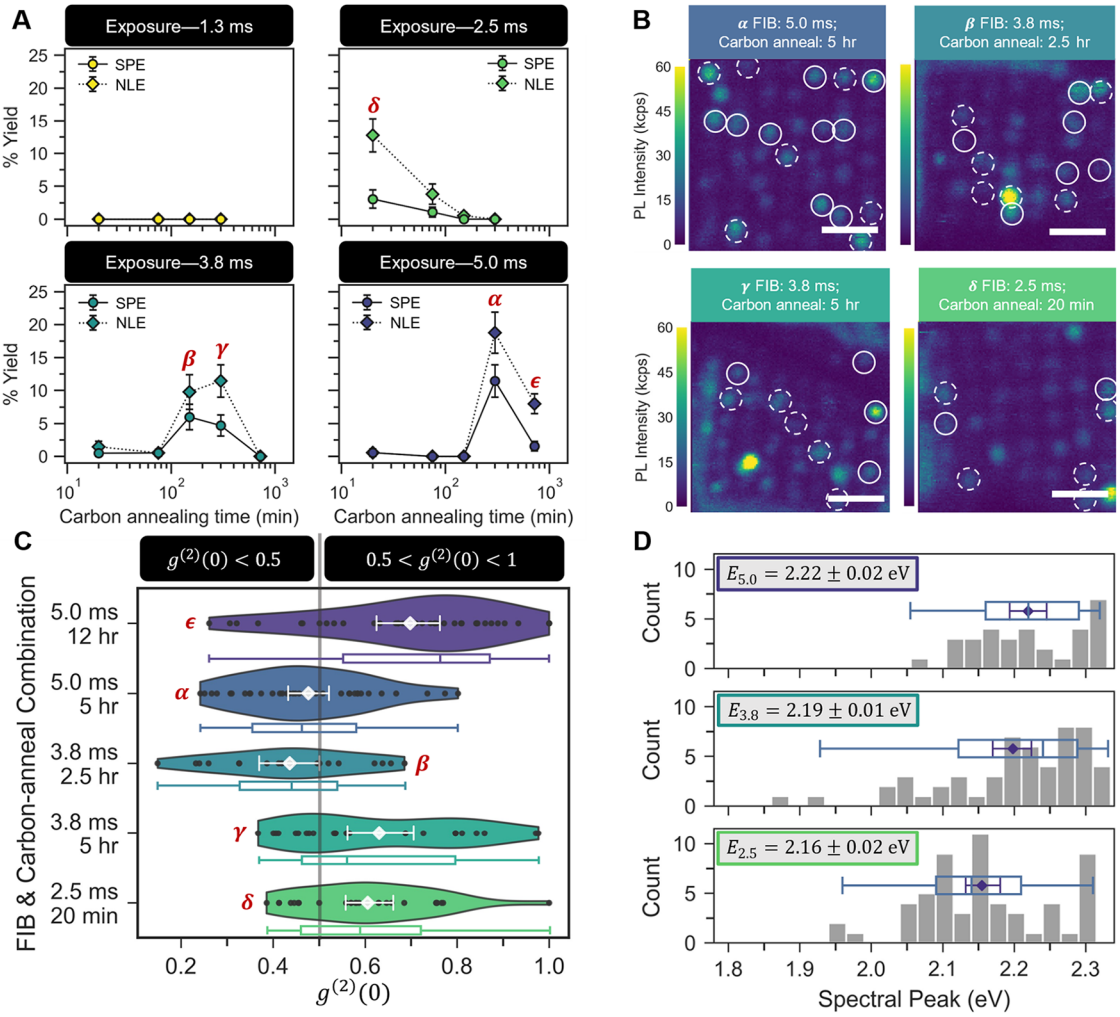

Figure 3. Tailoring SPE yield, $g^{(2)}(0)$, and emission energy. (A) Plots showing average SPE (yellow circles) and average NLE yield (green diamonds) for samples processed under the same optimization conditions. The conditions that on average produce the highest number of SPEs and NLEs are labeled with α being the conditions that produced the highest number of emitters on average, β the second highest, and so on. Error bars show standard error on the mean. (B) Representative confocal PL maps for the conditions that produce the 4 highest number of emitters on average. Scale bar: 2 μm (C) $g^{(2)}(0)$ value distribution for parameter combinations that yielded the most NLEs, where α, β, γ, δ, and ϵ labels correspond to the same labels in (A) and (B). White diamond with error bars for each experiment represents the average $g^{(2)}(0)$ and standard error on the mean. Dashed gray lines mark the SPE threshold $g^{(2)}(0) = 0.5$ (D) ZPL distribution by FIB exposure level. Purple diamond with error bars for each level represents average ZPL and standard error on the mean, listed in the colored box for each FIB exposure level. The standard deviation and inner quartile range (IQR) for 5.0, 3.8, and 2.5 ms FIB doses are $\sigma_{5.0} = 0.077$ and $IQR_{5.0} = [2.16,2.29]$ eV, $\sigma_{3.8} = 0.11$ eV and IQR = [2.11,2.28] eV, and $\sigma_{2.5} = 0.088$ and IQR = [2.09,2.21] eV, respectively.

The FIB exposure time was the only other main effect influencing the SPE yield, with "high" exposure (3.8 ms) producing 4× higher SPE yields than "low" exposure (2.5 ms) [Table S5 *F*-test: $p = 0.028$] [Figure 2D]. Surprisingly, annealing samples for 5 h did not produce a different SPE yield than annealing samples for 20 min [Table S5 *F*-test: $p = 0.544$].

When considering factor interactions, we found a strong interplay between the FIB exposure time and carbon anneal time: increasing the carbon anneal time boosted the SPE yield at high FIB exposure but reduced it at low exposure [Table S5, *F*-test: $p = 0.042$] [Figure 2E]. Moreover, this effect was amplified on thinner flakes but reversed on thicker ones, indicating a strong three-factor interaction among hBN thickness, FIB exposure time, and carbon anneal time [Table S5 *F*-test: $p = 0.005$] [Figure 2F].

Based on our factor screening results, the highest SPE yield occurs in thin hBN flakes (10−19 nm). However, a strong interaction between FIB exposure and carbon annealing time can significantly reduce the yield. To optimize our technique, we now explore the parameter space of FIB exposure and carbon annealing more closely. Since FIB introduces vacancy defects and CVD carbon annealing supplies carbon atoms, we hypothesize that maximizing SPE yield requires balancing the concentrations of vacancies and carbon impurities—an essential step in engineering carbon-based quantum emitters in pristine hBN.

OPTIMIZING SPE YIELD THROUGH DEFECT−IMPURITY BALANCE IN THIN HBN

To optimize emitter yield with this technique, we investigated the interaction between FIB exposure and carbon annealing across four exposure durations (1.3 ms, 2.5 ms, 3.8 ms, and 5 ms) and five annealing times (20, 75 , 150 , 300, and 720 min), spanning the range defined by the extremes used in the initial

https://doi.org/10.1021/acsami.5c16811
ACS Appl. Mater. Interfaces XXXX, XXX, XXX−XXX

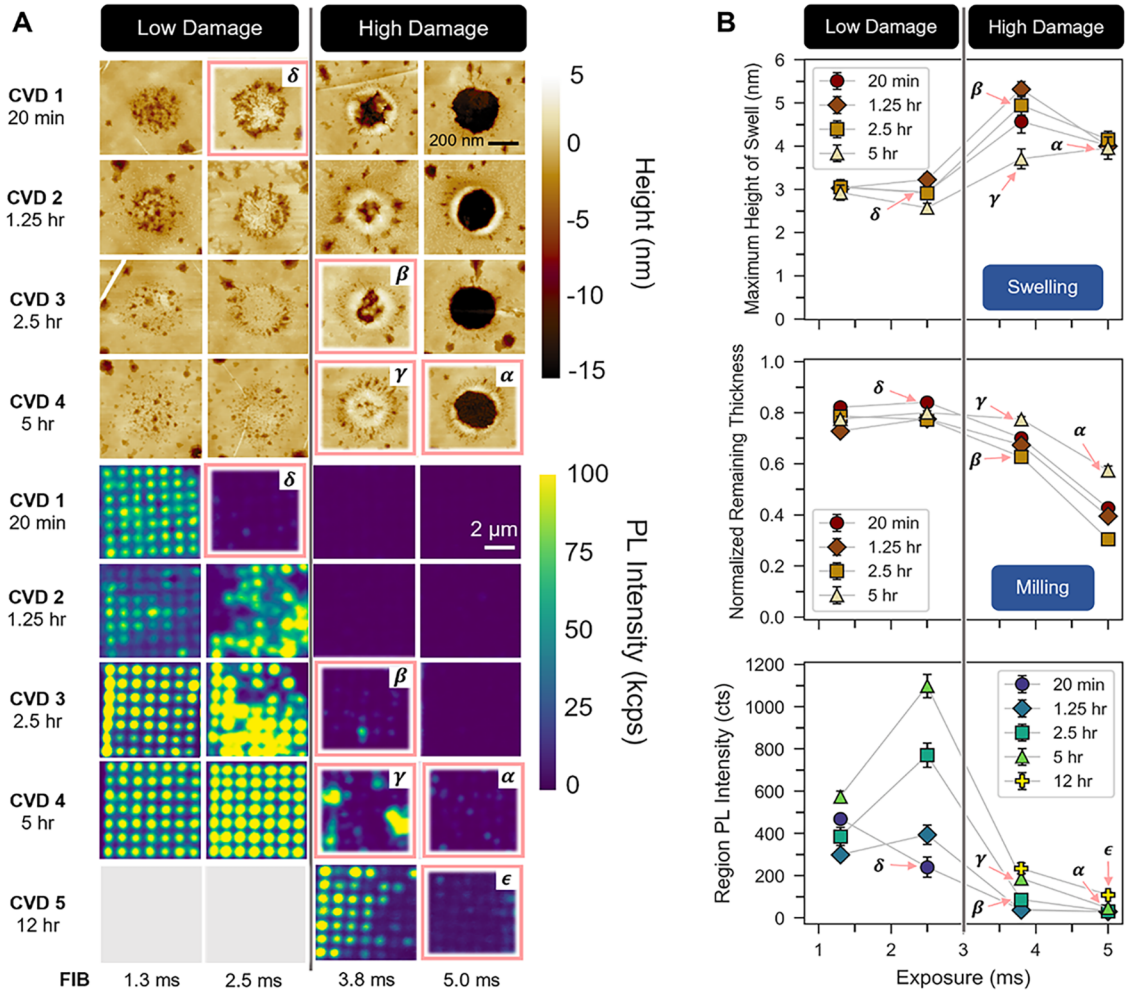

Figure 4. Atomic force microscopy and photoluminescence characterization. (A) Top: Array of AFM height scans of 500 nm holes patterned at all 4 FIB exposures and 4 carbon anneal times; Bottom: Array of 7 μm x 7 μm representative confocal PL scans for each combination of FIB exposure and carbon annealing times. (B) Top: Corresponding plots of average magnitude swell height and average normalized remaining thickness (calculated from mill depth) at each FIB exposure time calculated from AFM scans; Bottom: Interaction plot showing the average PL map intensity for each combination of FIB exposure and carbon annealing times. A, B, C, D labels correspond to the same FIB and carbon annealing combinations from Figure 3 for the conditions that produced the highest probability of NLEs. Error bars indicate the standard error of the mean. Data for CVD 4 reproduced from ref 16

factor screening. For these optimization experiments, we used hBN flakes with thicknesses between 11 and 18 nm and patterned circular features 500 nm in diameter. For more details about the experimental design, refer to the Methods section and Figure S8.

We observed that for short FIB exposure times, longer carbon annealing within our design space reduced SPE yield, while for longer exposures, the yield initially increased with annealing time, reached a peak, and then declined [Figure 3A]. This behavior generally agrees with the factor screening results. We found the highest SPE yields on regions exposed for 5.0 ms and annealed for 5 h, with an average SPE yield of 0.115 ± 0.009 SPEs/patterned site—approximately twice the yield produced by the best factor screening parameters [Table S8, Student's t test: $p < 0.0001$]. Of the many distinct experimental treatments, only five FIB exposure-carbon annealing time combinations yielded SPEs/NLEs at patterned sites [Table S7, Dunnett test with no FIB, no CVD control: $p < 0.001$], in order from highest to lowest SPE yield: (α) 5.0 ms:5 h, (β) 3.8 ms:2.5 h, (γ) 3.8 ms:5 h, (δ) 2.5 ms:20 min, (ϵ) 5.0 ms:12 h [Figure 3A,B].

While the current, most persistent need for integrating quantum emitters into photonic technologies is to optimize the yield of SPEs at deterministic locations, it is also essential to characterize the influence of the fabrication technique on optical characteristics, such as single photon purity and ZPL energy, that determine the utility of the emitters in these technologies. To determine if the particular combination of FIB exposure and carbon annealing times impacted the single photon purity, we characterized 157 emitters with $g^{(2)}(0) < 1$ on regions subjected to 12 of the 18 exposure and annealing combinations, with 65.6% of those emitters on regions subjected to the top five combinations listed above as producing the highest NLE yields. We found that emitters fabricated with conditions (α) and (β) had average $g^{(2)}(0) < 0.5$, while regions subjected to conditions (γ), (δ), and (ϵ) had average $g^{(2)}(0) > 0.5$ [Figure 3C]. Furthermore, we observed that at a fixed FIB exposure level, longer carbon annealing times led to higher average $g^{(2)}(0)$. This trend was evident across two pairs of treatments that shared the same FIB exposure but differed in the annealing duration. The $g^{(2)}(0)$ shift for the 3.8 ms FIB dose (β, γ pair) going from 3.5 to 5 h anneal was 0.20 ± 0.05, while the shift for the 5.0 ms dose (α,

https://doi.org/10.1021/acsami.5c16811
ACS Appl. Mater. Interfaces XXXX, XXX, XXX−XXX

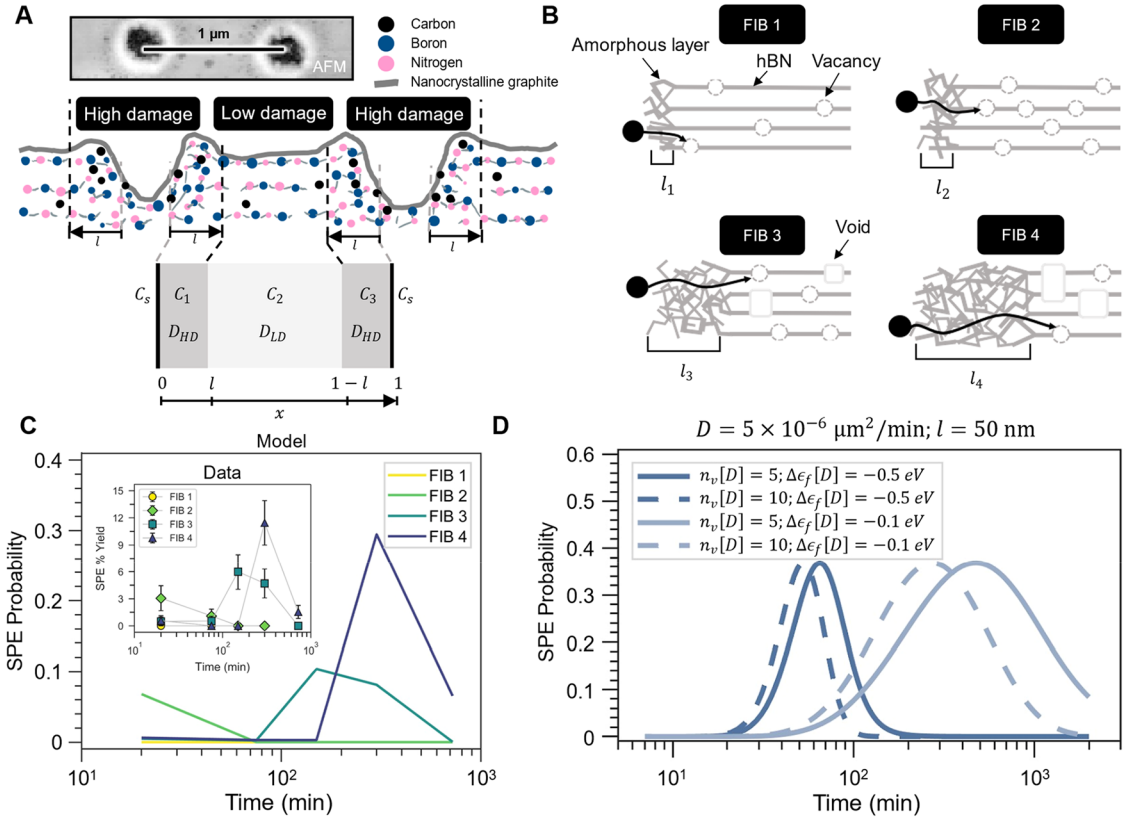

Figure 5. Model of physical mechanism for impurity diffusion and defect formation. (A) Sketch showing the region limits for multilayer diffusion model based on FIB damage, where labels are defined in main text. Inset: AFM image of FIB patterned holes showing swelling around edge region. (B) Sketch demonstrating how FIB-induced damage influences the number of potential color centers (and therefore dimmer or brighter PL) based on the conditions that impurity carbon must diffuse through for each FIB exposure level. (C) Plot of results from the evaluated model using a parameter set [Table S9] that reproduces the behavior we see in data for SPE yield at the tested anneal times. (D) Plot of results from the evaluated model showing labeled by variations to the default parameter set, demonstrating the dependence of the single color center creation probability (solid lines) and overall color center creation probability (dashed lines) on the high damage length and defect formation energy.

ϵ pair) was 0.22 ± 0.04 [Table S10]. These results demonstrate that we can tailor the quantum purity of emitters fabricated with this technique by adjusting the exposure time and the carbon annealing time.

To determine if we can similarly tailor the ZPL, we collected spectra from 143 color centers and observed ZPL within the expected visible range for hBN NLEs. We found that ZPL and ZPL distributions varied due to the FIB exposure time [Figure 3D]. Although the average ZPL of emitters patterned with the 3.8 ms (2.19 ± 0.01 eV, uncertainty is standard error; standard deviation $\sigma_{3.8}$ = 0.11 eV, inner quartile range (IQR) [2.11, 2.28] eV) and 5.0 ms (2.22 ± 0.02 eV, uncertainty is standard error; standard deviation $\sigma_{5.0}$ = 0.08 eV, IQR = [2.16, 2.29] eV) FIB exposure times were statistically similar [Table S11, *t*-test: p = 0.312], the average ZPL for emitters patterned with the 2.5 ms FIB level (2.16 ± 0.02 eV, uncertainty is standard error; standard deviation $\sigma_{2.5}$ = 0.09 eV, IQR = [2.09, 2.21] eV) differed from both the 3.8 and 5.0 ms FIB dose treatments [Table S11 3.8 ms-2.5 ms *t*-test: p = 0.016; 5.0 ms -2.5 ms *t*-test: p = 0.002]. This difference could indicate variations in the types of defects and defect complexes, local strain gradients, or substrate effects that are dependent on specific exposure and annealing combinations.

Results from our previous work using atomic force microscopy (AFM) to characterize surface morphology reveal that the four FIB exposure levels on a single sample (no variation in anneal time) show distinct differences in mill depth and swell/redeposition height, corresponding to differences in SPE yield and region PL.[20] Here, we extended this characterization and analysis to samples fabricated with the 20 min, 1.25, 2.5, and 5 h anneal times treatments to elucidate how FIB-induced damage may be influencing the structural environment for SPE formation and optical characteristics at different anneal times [Figure 4A].

In general, regions fabricated with the 3.8 and 5.0 ms FIB exposure times had higher swelling, deeper milling, and dimmer PL—regions we denote as "high damage"—than regions fabricated with the 1.3 and 2.5 ms exposure times—which we denote as "low damage" [Tables S13–S14, Tukey-Kramer HSD: $p < 0.0001$] [Figure 4B]. Consistent with our previous results for all but the 20 min anneal, PL got brighter first at the 2.5 ms exposure time before it got dimmer [Table S9, Tukey-Kramer HSD: $p < 0.0001$]; this peaking behavior is shown in the lower panel of Figure 4B. The 20 min anneal showed a PL that decreased monotonically with FIB exposure. Moreover, the 2.5 ms FIB exposure and 20 min anneal (treatment δ) were the only combination that produced SPEs in low damage samples [Table S7]. We conjecture that due to the longer exposure time compared to 1.3 ms exposure, the 2.5 ms exposed regions contained more surface damage not quantifiable as swelling or milling and therefore fewer atomic defects available near the surface to form color centers, thereby leading to isolated SPEs and dimmer PL overall at the shortest anneal time. This conjecture is supported by spectra acquired at sites where $g^{(2)}(0)$

https://doi.org/10.1021/acsami.5c16811
ACS Appl. Mater. Interfaces XXXX, XXX, XXX−XXX

> 0.5 having multiple ZPL or ZPL shapes characteristic of ensemble emission rather than single defect centers [Figure S9].

MULTILAYER DIFFUSION MODEL FOR DEFECT FORMATION

Carbon annealing is required for color center formation using our technique. The carbon that we deposit with this process must diffuse into the crystal and annihilate or bind with point vacancies and vacancy clusters created by FIB exposure. FIB exposure also creates high defect density regions that are extremely damaged, demonstrated by swelling due to amorphous binding, structural voids, and breakage. We expect that this damage changes the migration barrier E_b for impurity species in the material due to screening, trapping in voids, etc., thereby changing the diffusivity $D \propto e^{-E_b/k_B T}$ and ultimately the time it takes for impurities to diffuse through material ($t \propto 1/D$).

Based on our data showing regions patterned with longer FIB exposure (thereby sustaining high levels of damage) required longer anneal times to yield SPEs, we propose a multilayer diffusion model for the physical mechanism of defect formation where carbon diffuses through two distinct morphologies to form color centers, as described above and in Figure 4: (1) *High Damage*—a highly damaged morphology due to continuous, directed exposure leading to swelling and milling (D_{HD}) and (2) *Low Damage*—a lower damaged morphology due to the Gaussian tail of the FIB leading to overall lower dose exposure creating isolated vacancies (D_{LD}) [Figure 5A]. The Stopping and Range of Ions in Matter (SRIM) calculations from our previous work[20] show clear distinctions between high-defect concentration and low-defect concentration regions for each dose. We denote the dose-dependent characteristic lateral damage length as l_n [Figure 5B].

We model the carbon concentration $C(x,t)$ for a given FIB exposure level (the model configuration is shown in Figure 5A with constant l) via diffusion in composite media in one dimension,[21]

$$\frac{\partial C_i}{\partial t} = D_i \frac{\partial^2 C_i}{\partial x^2} \tag{1}$$

The indices i = 1,2,3 label the three damage regions with concentrations C_i and diffusivities $D_1 = D_3 = D_{HD}$ and $D_2 = D_{LD}$. The boundary conditions include perfect matching at interfaces

$$D_i \frac{\partial C_i}{\partial x}\bigg|_{l_-} = D_{i+1} \frac{\partial C_{i+1}}{\partial x}\bigg|_{l_+} \tag{2}$$

and constant surface concentration

$$C(0, t) = C_s \tag{3}$$

$$C(1, t) = C_s \tag{4}$$

where C_S is the surface concentration of nanocrystalline graphite deposited on the hBN surface during the anneal process.

For a specific color center with formation energy ΔE_f^D, the probability that an impurity carbon atom—at concentration $C(t)$—will combine with one of the N_v^D available vacancies to form a single, isolated SPE of that type follows a Boltzmann distribution

$$p_{SPE}(t) = \frac{\frac{N_v^D C(t)}{n_S} e^{-\beta \Delta E_f^D}}{1 + \sum_{n=1}^{N_v^D} \frac{1}{n!} \left(\frac{N_v^D C(t)}{n_S}\right)^n e^{-\beta n \Delta E_f^D}} \tag{5}$$

This model for the SPE yield predicts the experimentally observed behavior of longer carbon annealing producing higher SPE yields for high FIB exposure but lower yields for lower exposure [Figure 5C]. For more information about the calculations and system parameters used to evaluate the model, refer to Table S15 and Figure S11 of the Supporting Information.

The diffusion model, together with the morphological changes associated with increasing FIB dose,[20] sheds light on the following observation: for a fixed FIB dose, increasing the carbon deposition time generally produces commensurately brighter PL (Figure 4A and the lower panel of Figure 4B). This increase in PL, as well as the maximum PL, is greater at lower FIB doses than at higher doses within the parameter space of our experimental design. The origin of this difference is that a low FIB dose generates more isolated defects, while increasing the FIB dose causes these defects to coalesce, creating progressively larger voids in the hBN.[20] In the low-dose regime, the diffusion model predicts that increasing carbon deposition promotes carbon−defect complex formation and SPE activation, which, due to their high density, results in NLE behavior at best but generally very bright emission. In the high-dose regime, however, the number of isolated point defects available to generate SPEs is greatly reduced due to the prevalence of large voids, leading instead to dimmer PL with a higher probability of isolated SPEs. Taken together, these results highlight the interplay between FIB-induced morphology and carbon diffusion, revealing how tuning the dose and deposition time can steer the balance between brightness, emitter density, and isolation—key factors for optimizing reproducible SPE generation.

Furthermore, when we extended this multilayer diffusion model to untested anneal times, we observed that the anneal time corresponding to the SPE yield peak was highly dependent on the damage diffusion constant, the damage length, the number of vacancies available, and the defect formation energy but preserves the same qualitative behavior and saturates at the expected Poisson limit [Figure 5D]. Based on this result, we expect that the optimal annealing time for producing SPEs at the two lowest FIB exposure levels (1.3 ms and 2.5 ms) is less than 20 minutes, as those regions quickly reached supersaturation of color centers. Ultimately, we propose that SPE fabrication is most effective when annealing is timed to occur just before the onset of supersaturation, based on the known or calculated damage region length and vacancy concentration for a given FIB exposure level. Furthermore, a more comprehensive model that incorporates the formation energies of multiple defect types could yield a predictive value for this optimal annealing time, as defect formation energies strongly influence the time-dependent response of SPE probability.

DISCUSSION

To constrain the likely defects formed under our processing conditions, we refer to previous studies that have matched observed ZPLs to calculated ZPLs via density functional theory (DFT). Mendelson et al. put forth the $V_BC_N^-$ defect center as the source of observed visible range single photon emission with ZPL in the range of 585 ± 10 nm (2.12 eV),[13] while Fischer et al. favor the V_NC_B defect center with ZPL observed at 2.2 eV.[10] However, to date, the aforementioned defects remain controversial. For instance, our DFT calculations show that $V_BC_N^-$ is a spin-1/2 defect, and not a spin-3/2 defect as was calculated for a small few-ring flake of hBN.[13] Figure S14(B)

https://doi.org/10.1021/acsami.5c16811
ACS Appl. Mater. Interfaces XXXX, XXX, XXX−XXX

shows the defect formation energy for the V_BC_N defect in different charge states as a function of the electronic chemical potential. The two most favorable charge states are +1 and 0, both of which only first two are spin active, with spins 1/2 and 1, respectively, and so, this defect might not be the one observed in experiment by Mendelson et al. Also, according to our DFT calculations, the neutral V_NC_B is not spin active, with the nonmagnetic solution being the lower energy state, which was missed by earlier works.[22] Among the energetically most favorable charge states (+1 and 0) shown in Figure S14(C), only the +1 charge state is spin active and has a spin-1/2, which was also reported previously.[23] Additionally, our high-energy FIB exposure technique likely produces not only single point vacancies and divacancies, but also larger clusters, allowing a class of emitters that contain many carbons in a cluster.[24] One such defect candidate in the range of our observed emission is C_2C_N, modeled by Li et al. with a ZPL of 2.13 eV.[25] Figure S15 shows the formation energy reduction for this carbon cluster in the presence of vacancies in the hBN matrix.

We expect that defect candidates will vary based on the combination of FIB exposure and carbon annealing time due to differences in vacancy concentration, cluster size, and carbon concentration profile among the samples studied in this work. This is supported by the observed ZPL differences [Figure 3D]. Additionally, the structural environment within the 2.5 ms exposed regions is markedly different from the environment for the 3.8 and 5.0 ms exposed regions, altering the initial vacancy concentration and cluster size conditions, as well as local strain gradients and substrate interactions [Figure 4]. Furthermore, the SPEs fabricated with the 2.5 ms exposure time were possible only when annealed for the shortest time, while those created in the 3.8 and 5.0 ms exposed material were created with the highest carbon annealing times, directly impacting the total carbon dose available. While we cannot conclusively put forth a particular defect complex responsible for the emission we observe from SPEs fabricated with this technique, further characterization of the photophysics of these emitters such as polarization[26,27] and ODMR[11,24] as well as DFT and MD calculations for larger carbon-based defects could narrow the range of defect candidates possible for different combinations of FIB exposure and carbon doping levels and provide more information to elucidate the anneal time dynamics of color center creation.

There are further nontrivial limitations to elucidating a quantitative model for defect formation in FIB-exposed hBN doped via carbon diffusion. The Monte Carlo method used by SRIM to calculate ion-induced vacancy concentration does not fully account for sputtering and self-annealing,[28] whereas the sputtered volume and stability of large structural voids are important considerations in our study of optimal SPE creation. Additionally, evaluating the diffusion problem in more than one dimension would provide a more precise concentration model. Furthermore, the diffusion constants of carbon in hBN could be even more strongly dependent on the surrounding damage environment and vary not just between the high damage and low damage regimes but may be a continuous function of position $D(x)$ that is unique for each exposure level. However, comparing our results to this qualitative model allows us to constrain different testable regimes of FIB exposure and carbon annealing time to optimize and expand this fabrication technique, allowing for more refined control over the design of devices and selection of fabrication parameters to align with requirements for different hBN NLE-reliant applications.

Beyond hBN, many solid-state emission sources based on extrinsic defects benefit from adjustable patterning techniques. Many color centers in three-dimensional wide-bandgap materials such as diamond, GaN, and SiC—as well as defect-induced exciton transitions in two-dimensional transition metal dichalcogenides (TMDs)—rely on the controlled introduction of impurities to form defect complexes. However, current fabrication techniques often depend on specialized implantation systems, multistep photolithography to localize emitters, or both. The general technique presented in this work requires only the ability to first open a diffusion window and generate vacancies using FIB, followed by the introduction of impurity dopants through CVD or annealing—relying on equipment and resources commonly available in standard fabrication facilities. Although other single photon sources are based on different extrinsic defect complexes—such as NV in diamond, $V_{Si}V_C$ in 4H-SiC,[29] Cr_w in WS_2[30]—impurity sources and concentrations can be tuned by adjusting the dopant feedstock gas or introducing a precursor upstream. Simultaneously, FIB patterning parameters can be tailored to control vacancy concentrations and enable impurity incorporation through a high damage diffusion barrier. Broad application of this technique for patterning solid-state single photon emitters could unlock scalable integration of quantum emitters into photonic and sensing platforms, offering unique advantages in precision, performance, and functionality.

CONCLUSIONS

In this work, we engineered single photon sources in pristine hBN by combining FIB patterning and carbon diffusion via CVD of nanocrystalline graphite as a carbon source. By exploring a portion of the rich parameter space of this technique, we found multiple combinations of FIB exposure dose and diffusion time that successfully created SPEs and determined that crystals with thickness ∼15 nm, FIB exposure for 5.0 ms, and carbon annealing for 5 h lead to the highest yield of SPEs, with other combinations providing a means to produce SPEs with different average purity and ZPL range. Furthermore, by analyzing AFM and confocal PL images of hBN regions treated with 18 different combinations of the FIB exposure dose and carbon diffusion time, we revealed that carbon impurities likely diffuse through highly damaged, swollen layers to activate color centers. Additionally, simulations using SRIM and a multilayer diffusion model revealed that less damaged regions require shorter, more precisely timed diffusion—on the order of minutes, while more heavily damaged regions tolerate longer, less precise diffusion, on the order of hours. These results enabled us to define a method for constraining the optimal diffusion time range needed to generate SPEs for a given level of FIB-induced damage.

Together with DFT calculations and future work to characterize the polarization and spin properties of these patterned emitters, our results pave the way for precise spatial and chemical control over defect formation. This advancement could significantly enhance the scalability and applicability of hBN single photon emitter integration across a wide range of quantum information technologies. Moreover, the scalability and tunability of our technique make it adaptable to other low-defect materials beyond hBN, with exposure dose, impurity species, and diffusion time tailored to specific system requirements and fabrication constraints. This approach establishes a versatile fabrication framework for designing and integrating both monolithic and hybrid quantum systems, enabling efficient

https://doi.org/10.1021/acsami.5c16811
ACS Appl. Mater. Interfaces XXXX, XXX, XXX−XXX

coupling of single photons for quantum transduction, communication, and sensing using tools and processes accessible in standard fabrication environments.

METHODS

Sample Fabrication. *All Experiments.* The samples studied were prepared on Si wafers with 300 nm of thermal wet oxide from the University Wafer. Wafers were diced into 7 mm × 7 mm chips and patterned with a number array via laser writing and reactive ion etching for labeling purposes only. After the labeling process, chips were cleaned in an acetone sonication bath for 5 min and an IPA sonication bath for 5 min. Cleaned chips were exposed to 300 mTorr O_2 plasma at 300 W RF power in a March plasma cleaner for 1 min to create a hydrophilic surface for material transfer adhesion. HPHT hBN crystals were prepared for exfoliation transfer on a thermal release tape. The thermal release tape with hBN crystals was placed on the chip surface immediately after the oxygen plasma exposure. The chip-hBN-tape stack was placed on a 120 °C hot plate for 5 min to release the tape from the chip-hBN stack. The sample was cleaned of any tape residue in a tube furnace open to air at 500 °C for 3 h with no gas flow.

FIB Only, FIB+CVD Experiments. FIB exposure to create vacancy and edge defects occurred in an FEI Helios Dual Beam with a gallium ion source. Prior to sample loading, the chamber was plasma cleaned with air for 5 min. The FIB was set to an acceleration voltage of 20 keV and a beam current of 59 pA. The circular pattern exposure mask was drawn directly in the FIB window of the execution software interface with a desired circle diameter of either 250 or 500 nm depending on the experiment. Once the pattern was drawn in the software, an array of circle patterns with a 1 μm pitch was made. The exposure time was set in the pattern settings of the execution software to 1.3, 2.5, 3.8, or 5.0 ms depending on the experiment. When the desired hBN flake was located via SEM, the FIB pattern was executed, exposing only the regions of the material as determined in the circular array pattern exposure mask.

CVD Only, FIB+CVD Experiments. Samples immediately underwent the CVD process to introduce carbon into the crystal environment. Samples were loaded into the tube furnace connected to a vacuum system, and the system was evacuated to a base pressure of ∼30 mTorr. When the base pressure was reached, the C_2H_4, Ar, and H_2 gas lines were purged. Once the base pressure was reached again, the furnace temperature set point was ramped to 1000 °C over 30 min under 50 sccm Ar. After 40 min, the temperature was held at 1000 °C for 20, 75, 150, or 300 min depending on the experiment. During this time, the gas flow was 35 sccm ethylene, 2 sccm H_2, and 5 sccm Ar at 1 Torr. At the end of the designated time, the furnace temperature set point was set to 0 °C and the sample was allowed to gradually cool under 50 sccm Ar. When the temperature readout reached 400 °C, the furnace lid was opened to speed up the rest of the cooling process. The CVD process was ended when the temperature readout reached 200 °C. The vacuum system was vented, and samples were removed.

FIB Only, CVD Only, and FIB+CVD Experiments. To remove residual carbon on the surface, the samples underwent a cleaning anneal at 850 °C for 30 min under 5 scfh O_2.

Characterization. *Atomic Force Microscopy.* After material transfer and 500 °C cleaning anneal, the hBN flake thickness was characterized by taking a line cut measurement of a few micrometer square area AFM image taken via Bruker Dimension FastScan AFM in Tapping Mode. After the full fabrication process, AFM images of the FIB-exposed regions were also taken via a Bruker Dimension FastScan AFM in Tapping Mode. From the AFM data, we can acquire the average mill depth ($-\Delta z$ from unmilled material to the lowest point in the exposed circle area) and the average swell or redeposition height ($+\Delta z$) from unmilled material to the highest point in the exposed circle area for samples exposed by FIB for each exposure time tested. The analysis technique used is outlined in a previous work by the authors.[20]

Optical Characterization. Confocal PL images were taken to identify spots of photoluminescence in a home-built confocal microscope with 532 nm solid-state laser (OptoEngine) excitation, 100× 0.7 NA objective, dichroic beam splitter, and 550 nm long pass filter. Emission was coupled to a ThorLabs fiber optic 50:50 beam splitter, and photon counts for each path were detected by avalanche photodiodes (Micro Photon Devices). PL images show the signal from one APD. Time correlated photon counting was performed in a Hanbury-Brown and Twiss experiment using the signal from both APDs sent to a PicoQuant TimeHarp 260. These measurements were used to determine if PL sources were NLEs, and also yielded their average photon number, nonradiative and radiative lifetimes, and bunching amplitude. These parameters were extracted from antibunching measurements by fitting our data to the following second-order correlation function model for a three-level system:

$$g^{(2)}(t) = 1 - \rho^2 + \rho^2(1 - (1 - a)e^{-|t|/\tau_1} + ae^{-|t|/\tau_2}) \quad (6)$$

where a is the bunching amplitude, τ_1 is the nonradiative lifetime, τ_2 is the radiative lifetime, and $\rho^2 = 1 - g^{(2)}(0)$, where $g^{(2)}(0)$ is the degree of antibunching. Photon number in a given milled hole was determined by binning $g^{(2)}(0)$ values according to

$$g^{(2)}(0) = 1 - \frac{1}{n} \quad (7)$$

PL spectra of emitting sites and Raman spectra of the material were collected in a commercial WITec alpha300 spectrometer equipped with a Peltier-cooled Andor iDus CCD.

Statistical Analysis. Characterized regions were divided into 4 μm^2 segments, which corresponds to 4 FIB patterned locations for patterned samples because we patterned exactly one circle per 1 μm^2. To calculate mean SPE (NLE) density or yield, we recorded the number of emission sites with $g^{(2)}(0) < 0.5$ ($g^{(2)}(0) < 1$) in each 4 μm^2 region and averaged all regions processed with a given combination of experimental input factors. To calculate the mean PL map intensity, we converted all confocal image points from kcps to cts by the detection bin size of 0.1 s and plotted in grayscale, where 0 corresponded to the minimum counts value and 255 corresponded to the maximum counts value for the given PL map. We recorded the mean pixel height in ImageJ for each region, converted it to the mean PL intensity in counts, and averaged all regions processed with a given combination of experimental input factors. To elucidate which input factors influence successful SPE creation alone or combined with other input factors and obtain significance values, we performed a Full Model Effects Test on the number of SPEs counted, number of NLEs counted, and average PL in each 4 μm^2 region.

All statistical tests were performed in SAS JMP 15.1 statistical analysis software. Factor Screening (4-factor 2-level) Full Model Effects Test and all ANOVA tests (test specified in main text, i.e., Student's t test, Tukey-Kramer, or Dunnett test) were performed with significance level $\alpha = 0.05$. Prior to all statistical tests for SPE Yield, NLE Yield, and Region PL Counts, we performed a variance stabilizing transform for Poissonian data:

$$\tilde{x} = \sqrt{x} \quad (8)$$

Multilayer Diffusion Defect Formation Model. We employed the semianalytical solution to the multilayer diffusion problem based on the Laplace transform eigenfunction expansion and corresponding MATLAB code made available by Carr and Turner[21] to solve for $C_i(x,t)$ at each anneal time. Parameter values for diffusivities and damage lengths were determined by order-of-magnitude estimations informed in the literature, previous work, and data and can be found in Table S9.

We determined an estimate for N_v^D at each tested exposure dose using SRIM calculations convolved with AFM linecuts from ref 18 and assuming that of all of the calculated point vacancies and vacancy complexes, only a small percentage (∼1%) would 1 have a formation energy low enough to form a defect complex with carbon and 2 when the complex is formed, would be optically active under 532 nm excitation. $p_{SPE}(t)$ to produce Figure 5C,D were calculated in MATLAB using the evaluated solutions for $C_i(x,t)$.

Ab Initio Calculations. Spin-polarized DFT calculations were performed within the generalized gradient approximation[31] of Perdew−Burke−Ernzerhof[32] as implemented in the Quantum Espresso package.[33] We used 6 × 6 × 1 (72-atoms) and 12 × 12 × 1 (288-atoms) supercells of hBN in the calculations. The Brillouin zone was sampled at the Γ-point for the larger supercell, while a Γ-centered, 4 × 4 × 1 k-grid,

https://doi.org/10.1021/acsami.5c16811
ACS Appl. Mater. Interfaces XXXX, XXX, XXX−XXX

created within the Monkhorst−Pack scheme,[34] was used for the smaller supercell. A 20 Å vacuum layer was added in the direction normal to the hBN surface, ensuring minimal interactions between periodic images in the *z*-direction. The formation energies of the defects were calculated using the CoFFEE[35] code, which implements the Freysoldt-Neugebauer-Van De Walle (FNV) correction scheme[36] to remove the spurious interactions between a charged defect and its images.[36]

■ ASSOCIATED CONTENT

Data Availability Statement

The data that support the findings of this study are available from the corresponding author upon reasonable request.

Supporting Information

The Supporting Information is available free of charge at https://pubs.acs.org/doi/10.1021/acsami.5c16811.

Additional experimental and theoretical details, materials, methods, and data, including Raman characterization of graphite deposition, pattern localization data, factorial screening experiments, and data tables, ANOVA full model effects test and means plots, single photon emitter yield optimization data, ZPL characterization, AFM characterization, multilayer diffusion model, color center yield calculation, and ab initio DFT results (PDF)

■ AUTHOR INFORMATION

Corresponding Author

Benjamín J. Alemán − *Department of Physics; Material Science Institute; Center for Optical, Molecular, and Quantum Science, University of Oregon, Eugene, Oregon 97403, United States; Phil and Penny Knight Campus for Accelerating Scientific Impact, University of Oregon, Eugene, Oregon 97403, United States;* orcid.org/0000-0002-7976-4235; Email: baleman@uoregon.edu

Authors

Rachael Klaiss − *Department of Physics; Material Science Institute; Center for Optical, Molecular, and Quantum Science, University of Oregon, Eugene, Oregon 97403, United States*

Joshua Ziegler − *Department of Physics; Material Science Institute; Center for Optical, Molecular, and Quantum Science, University of Oregon, Eugene, Oregon 97403, United States;* orcid.org/0000-0001-7355-3149

David J. Miller − *Department of Physics; Material Science Institute; Center for Optical, Molecular, and Quantum Science, University of Oregon, Eugene, Oregon 97403, United States*

Kara Zappitelli − *Department of Physics; Material Science Institute; Center for Optical, Molecular, and Quantum Science, University of Oregon, Eugene, Oregon 97403, United States*

Kenji Watanabe − *Research Center for Functional Materials, National Institute for Materials Science, Tsukuba 305-0044, Japan;* orcid.org/0000-0003-3701-8119

Takashi Taniguchi − *International Center for Materials Nanoarchitectonics, National Institute for Materials Science, Tsukuba 305-0044, Japan;* orcid.org/0000-0002-1467-3105

Sai Krishna Narayanan − *Department of Physics and Astronomy, Howard University, Washington, District of Columbia. 20059, United States;* orcid.org/0000-0003-1420-4488

Pratibha Dev − *Department of Physics and Astronomy, Howard University, Washington, District of Columbia. 20059, United States;* orcid.org/0000-0002-6884-6737

Complete contact information is available at: https://pubs.acs.org/10.1021/acsami.5c16811

Author Contributions

R.K. and B.A. conceived and designed the experiment. R.K. fabricated and characterized samples, performed computational simulations, and analyzed the data. J.Z. developed the initial dose and energy factor levels for FIB milling. D.M. and K.Z. designed and built the CVD platform used for carbon-rich annealing. K.W. and T.T. synthesized the HPHT hBN crystals. S.K.N. and P.D. performed ab initio calculations. R.K., S.K.N., P.D., and B.A. cowrote the manuscript. All authors reviewed the manuscript. B.A. supervised the work.

Notes

The authors declare no competing financial interest.

■ ACKNOWLEDGMENTS

The authors thank Brittany Carter, Uriel Hernandez, Viva Horowitz, and Chris Hendon for discussion of this work. The authors thank Bri McAllister for creating the Table of Contents graphic. This work was supported by the University of Oregon, the Reneé James Seed Grant Initiative, and the National Science Foundation (NSF) under grant No. CMMI-2128671 and No. OMA-2231278. R.K., J.Z., D.M., K.Z., and B.A. acknowledge facilities and staff at the Center for Advanced Materials Characterization in Oregon, and the use of the University of Oregon's Rapid Materials Prototyping facility, funded by the Murdock Charitable Trust. K.W. and T.T. acknowledge support from JSPS KAKENHI (Grant Numbers 19H05790, 20H00354, and 21H05233). S.K.N. and P.D. were supported by the National Science Foundation (NSF grants no. DMR-1752840 and no. OMA-2231278). This work used the Expanse and Bridges2 clusters at SDSC and PSC, respectively, through allocation PHY180014 from the Advanced Cyberinfrastructure Coordination Ecosystem: Services & Support (ACCESS) program, which is supported by National Science Foundation grants No. 2138259, No. 2138286, No. 2138307, No. 2137603, and No. 2138296.

■ REFERENCES

(1) Kimble, H. J. The Quantum Internet. *Nature* **2008**, *453* (7198), 1023−1030.

(2) Moody, G.; Sorger, V. J.; Blumenthal, D. J.; Juodawlkis, P. W.; Loh, W.; Sorace-agaskar, C.; Jones, A. E.; Balram, K. C.; Matthews, J. C. F.; Laing, A.; Davanco, M.; Chang, L.; Bowers, J. E.; Quack, N.; Galland, C.; Aharonovich, I.; Wolff, M. A.; Schuck, C.; Sinclair, N.; Lon, M.; Komljenovic, T.; Weld, D.; Mookherjea, S.; Buckley, S.; Radulaski, M.; Reitzenstein, S.; Pingault, B.; Machielse, B.; Mukhopadhyay, D.; et al. 2022 Roadmap on Integrated Quantum Photonics. *J. Phys. Photonics* **2022**, *4*, No. 012501.

(3) Kaur, P.; Boes, A.; Ren, G.; Nguyen, T. G.; Roelkens, G.; Mitchell, A. Hybrid and Heterogeneous Photonic Integration. *APL Photonics* **2021**, *6* (6), No. 061102.

(4) Zhang, G.; Cheng, Y.; Chou, J. P.; Gali, A. Material Platforms for Defect Qubits and Single-Photon Emitters. *Appl. Phys. Rev.* **2020**, *7* (3), No. 031308.

(5) Aharonovich, I.; Englund, D.; Toth, M. Solid-State Single-Photon Emitters. *Nat. Photonics* **2016**, *10* (10), 631−641.

(6) Kianinia, M.; Xu, Z. Q.; Toth, M.; Aharonovich, I. Quantum Emitters in 2D Materials: Emitter Engineering, Photophysics, and Integration in Photonic Nanostructures. *Appl. Phys. Rev.* **2022**, *9* (1), No. 011306.

(7) Schell, A. W.; Takashima, H.; Tran, T. T.; Aharonovich, I.; Takeuchi, S. Coupling Quantum Emitters in 2D Materials with Tapered Fibers. *ACS Photonics* **2017**, *4* (4), 761−767.

(8) Tran, T. T.; Zachreson, C.; Berhane, A. M.; Bray, K.; Sandstrom, R. G.; Li, L. H.; Taniguchi, T.; Watanabe, K.; Aharonovich, I.; Toth, M. Quantum Emission from Defects in Single-Crystalline Hexagonal Boron Nitride. *Phys. Rev. Appl.* **2016**, *5* (3), No. 034005.
(9) Aharonovich, I.; Tetienne, J. P.; Toth, M. Quantum Emitters in Hexagonal Boron Nitride. *Nano Lett.* **2022**, *22* (23), 9227−9235.
(10) Fischer, M.; Caridad, J. M.; Sajid, A.; Ghaderzadeh, S.; Ghorbani-Asl, M.; Gammelgaard, L.; Bøggild, P.; Thygesen, K. S.; Krasheninnikov, A. V.; Xiao, S.; Wubs, M.; Stenger, N. Controlled Generation of Luminescent Centers in Hexagonal Boron Nitride by Irradiation Engineering. *Sci. Adv.* **2021**, *7* (8), No. 7138.
(11) Kianinia, M.; White, S.; Fröch, J. E.; Bradac, C.; Aharonovich, I. Generation of Spin Defects in Hexagonal Boron Nitride. *ACS Photonics* **2020**, *7* (8), 2147−2152.
(12) Xu, Z. Q.; Elbadawi, C.; Tran, T. T.; Kianinia, M.; Li, X.; Liu, D.; Hoffman, T. B.; Nguyen, M.; Kim, S.; Edgar, J. H.; Wu, X.; Song, L.; Ali, S.; Ford, M.; Toth, M.; Aharonovich, I. Single Photon Emission from Plasma Treated 2D Hexagonal Boron Nitride. *Nanoscale* **2018**, *10* (17), 7957−7965.
(13) Mendelson, N.; Chugh, D.; Reimers, J. R.; Cheng, T. S.; Gottscholl, A.; Long, H.; Mellor, C. J.; Zettl, A.; Dyakonov, V.; Beton, P. H.; Novikov, S. V.; Jagadish, C.; Tan, H. H.; Ford, M. J.; Toth, M.; Bradac, C.; Aharonovich, I. Identifying Carbon as the Source of Visible Single-Photon Emission from Hexagonal Boron Nitride. *Nat. Mater.* **2021**, *20* (3), 321−328.
(14) Horder, J.; White, S.; Gale, A.; Li, C.; Watanabe, K.; Taniguchi, T.; Kianinia, M.; Aharonovich, I.; Toth, M. Coherence Properties of Electron Beam Activated Emitters in Hexagonal Boron Nitride under Resonant Excitation. *Phys. Rev. Appl.* **2022**, *18* (6), No. 064021.
(15) Xu, X.; Martin, Z. O.; Sychev, D.; Lagutchev, A. S.; Chen, Y. P.; Taniguchi, T.; Watanabe, K.; Shalaev, V. M.; Boltasseva, A. Creating Quantum Emitters in Hexagonal Boron Nitride Deterministically on Chip-Compatible Substrates. *Nano Lett.* **2021**, *21* (19), 8182−8189.
(16) Ziegler, J.; Klaiss, R.; Blaikie, A.; Miller, D.; Horowitz, V. R.; Alemán, B. J. Deterministic Quantum Emitter Formation in Hexagonal Boron Nitride via Controlled Edge Creation. *Nano Lett.* **2019**, *19* (3), 2121−2127.
(17) Benedek, Z.; Babar, R.; Ganyecz, Á.; Szilvási, T.; Legeza, Ö.; Barcza, G.; Ivády, V. Symmetric Carbon Tetramers Forming Spin Qubits in Hexagonal Boron Nitride. *NPJ. Comput. Mater.* **2023**, *9* (1), No. 187.
(18) Korona, T.; Jankowska, J.; Masoumifeshani, E. Dicarbon Defect in Hexagonal Boron Nitride Monolayer—a Theoretical Study. *Can. J. Chem.* **2023**, *101* (9), 684−697.
(19) Lyu, C.; Zhu, Y.; Gu, P.; Qiao, J.; Watanabe, K.; Taniguchi, T.; Ye, Y. Single-Photon Emission from Two-Dimensional Hexagonal Boron Nitride Annealed in a Carbon-Rich Environment. *Appl. Phys. Lett.* **2020**, *117* (24), No. 244002.
(20) Klaiss, R.; Ziegler, J.; Miller, D.; Zappitelli, K.; Watanabe, K.; Taniguchi, T.; Alemán, B. Uncovering the Morphological Effects of High-Energy Ga+focused Ion Beam Milling on HBN Single-Photon Emitter Fabrication. *J. Chem. Phys.* **2022**, *157* (7), No. 074703.
(21) Carr, E. J.; Turner, I. W. A Semi-Analytical Solution for Multilayer Diffusion in a Composite Medium Consisting of a Large Number of Layers. *Appl. Math. Modell.* **2016**, *40* (15−16), 7034−7050.
(22) Tawfik, S. A.; Ali, S.; Fronzi, M.; Kianinia, M.; Tran, T. T.; Stampfl, C.; Aharonovich, I.; Toth, M.; Ford, M. J. First-Principles Investigation of Quantum Emission from HBN Defects. *Nanoscale* **2017**, *9* (36), 13575−13582.
(23) Abdi, M.; Chou, J. P.; Gali, A.; Plenio, M. B. Color Centers in Hexagonal Boron Nitride Monolayers: A Group Theory and Ab Initio Analysis. *ACS Photonics* **2018**, *5* (5), 1967−1976.
(24) Li, S.; Pershin, A.; Thiering, G.; Udvarhelyi, P.; Gali, A. Ultraviolet Quantum Emitters in Hexagonal Boron Nitride from Carbon Clusters. *J. Phys. Chem. Lett.* **2022**, *13*, 3150−3157.
(25) Li, K.; Smart, T. J.; Ping, Y. Carbon Trimer as a 2 EV Single-Photon Emitter Candidate in Hexagonal Boron Nitride: A First-Principles Study. *Phys. Rev. Mater.* **2022**, *6* (4), No. L042201.
(26) Bommer, A.; Becher, C. New Insights into Nonclassical Light Emission from Defects in Multi-Layer Hexagonal Boron Nitride. *Nanophotonics* **2019**, *8* (11), 2041−2048.
(27) Gu, R.; Wang, L.; Zhu, H.; Han, S.; Bai, Y.; Zhang, X.; Li, B.; Qin, C.; Liu, J.; Guo, G.; Shan, X.; Xiong, G.; Gao, J.; He, C.; Han, Z.; Liu, X.; Zhao, F. Engineering and Microscopic Mechanism of Quantum Emitters Induced by Heavy Ions in HBN. *ACS Photonics* **2021**, *8* (10), 2912−2922.
(28) Ziegler, J. F.; Ziegler, M. D.; Biersack, J. P. SRIM - The Stopping and Range of Ions in Matter. *Nucl. Instrum. Methods Phys. Res. B* **2010**, *268* (11−12), 1818−1823.
(29) Li, Q.; Wang, J.-F.; Yan, F.-F.; Zhou, J.-Y.; Wang, H.-F.; Liu, H.; Guo, L.-P.; Zhou, X.; Gali, A.; Liu, Z.-H.; Wang, Z.-Q.; Sun, K.; Guo, G.-P.; Tang, J.-S.; Li, H.; You, L.-X.; Xu, J.-S.; Li, C.-F.; Guo, G.-C. Room-Temperature Coherent Manipulation of Single-Spin Qubits in Silicon Carbide with a High Readout Contrast. *Natl. Sci. Rev.* **2022**, *9* (5), No. nwab122.
(30) Schuler, B.; Lee, J. H.; Kastl, C.; Cochrane, K. A.; Chen, C. T.; Refaely-Abramson, S.; Yuan, S.; Van Veen, E.; Roldán, R.; Borys, N. J.; Koch, R. J.; Aloni, S.; Schwartzberg, A. M.; Ogletree, D. F.; Neaton, J. B.; Weber-Bargioni, A. How Substitutional Point Defects in Two-Dimensional WS2 Induce Charge Localization, Spin-Orbit Splitting, and Strain. *ACS Nano* **2019**, *13* (9), 10520−10534.
(31) Perdew, J. P.; Yue, W. Accurate and Simple Density Functional for the Electronic Exchange Energy: Generalized Gradient Approximation. *Phys. Rev. B* **1986**, *33* (12), No. 8800.
(32) Perdew, J. P.; Burke, K.; Ernzerhof, M. Generalized Gradient Approximation Made Simple. *Phys. Rev. Lett.* **1996**, *77* (3), No. 3865.
(33) Giannozzi, P.; Baroni, S.; Bonini, N.; Calandra, M.; Car, R.; Cavazzoni, C.; Ceresoli, D.; Chiarotti, G. L.; Cococcioni, M.; Dabo, I.; Corso, A. D.; Gironcoli, S. De.; Fabris, S.; Fratesi, G.; Gebauer, R.; Gerstmann, U.; Gougoussis, C.; Kokalj, A.; Lazzeri, M.; Martin-Samos, L.; Marzari, N.; Mauri, F.; Mazzarello, R.; Paolini, S.; Pasquarello, A.; Paulatto, L.; Sbraccia, C.; Scandolo, S.; Sclauzero, G.; Seitsonen, A. P.; Smogunov, A.; Umari, P.; Wentzcovitch, R. M. QUANTUM ESPRESSO: A Modular and Open-Source Software Project for Quantum Simulations of Materials. *J. Phys.: Condens. Matter* **2009**, *21*, No. 395502.
(34) Monkhorst, H. J.; Pack, J. D. Special Points for Brillouin-Zone Integrations. *Phys. Rev. B* **1976**, *13* (12), No. 5188.
(35) Naik, M. H.; Jain, M. CoFFEE: Corrections For Formation Energy and Eigenvalues for Charged Defect Simulations. *Comput. Phys. Commun.* **2018**, *226*, 114−126.
(36) Freysoldt, C.; Neugebauer, J.; Van De Walle, C. G. Fully Ab Initio Finite-Size Corrections for Charged-Defect Supercell Calculations. *Phys. Rev. Lett.* **2009**, *102* (1), No. 016402, DOI: 10.1103/PhysRevLett.102.016402.

https://doi.org/10.1021/acsami.5c16811
ACS Appl. Mater. Interfaces XXXX, XXX, XXX−XXX